Impact mechanisms of debris flow on barriers: modelling, analysis and design

Ng, C.W.W.[1], Choi, C.E.[2], Liu, H.[1], Wang, C.[1], and Kwan, J.S.H.[3]

[1]*Department of Civil and Environmental Engineering, the Hong Kong University of Science and Technology, HKSAR, China*

[2]*Department of Civil Engineering, The University of Hong Kong, HKSAR, China*

[3]*Civil Engineering and Development Department, Geotechnical Engineering Office, HKSAR, China*

Charles.Ng@ust.hk

Abstract

Debris flows pose a significant threat to sustainable development in mountainous areas, including those in Colombia and Hong Kong. To protect lives and facilities against these hazardous flows, rigid barriers are commonly installed in channels. Deformable barriers have proven to be effective at reducing the impact force exerted by debris flows. Barriers are essentially designed empirically because not much is known about their fundamental impact mechanisms. In this keynote paper, physical experiments that model dry sand, water and two-phase debris flows impact on a rigid barrier are presented. Experiments were conducted using a 5 m-long flume and a 28 m-long flume to address the scale-dependant nature of debris flows. A calibrated numerical model using the Material Point Method was then adopted to carry out a parametric study to shed light on the effects of barrier flexural rigidity on the impact force exerted by granular flow. Based on the experimental and numerical results, design recommendations are provided.

1 INTRODUCTION

Debris flows, mixtures of soil and water, surge downslope at high velocities. These flows often result in fatalities and damage to infrastructure. To arrest debris flows, rigid barriers are installed in channels (Fig. 1). Over recent decades, research has shown that barriers that deform upon impact can be even more effective at reducing the impact forces (Ng et al. 2017a; Ng et al. 2020a).

In existing international design guidelines (Kwan 2012; Volkwein 2014), the total impact force exerted by a debris flow can be expressed as follows:

$$F_{\text{peak}} = \alpha \rho v^2 h_0 w + 0.5 k \rho g h_0^2 w \qquad (1)$$

where α and k are the dynamic and static impact coefficients, respectively; ρ is the flow density; v is the velocity of the flow; h_0 is the flow depth and w is the channel width. In Hong Kong, α is recommended to be 2.5 for rigid barriers (Kwan 2012) and 2.0 for flexible barriers (Kwan and Cheung 2012). Such large α values were recommended to account for the hard and large inclusions in debris flows. Additionally, k = 1.0 is adopted by assuming that the flow has negligible shear strength (NILIM 2007; Kwan and Cheung 2012; Volkwein 2014). However, these recommendations have been demonstrated to be over-conservative (Ng et al. 2020b; 2021) and there is room to improve the estimation of design impact forces to optimise the design of barriers.

Our current knowledge on flow-barrier interaction is deficient because: (*i*) the fundamental mechanisms of impact between debris flows and barriers are rarely captured in the field; (*ii*) debris flows are scale-dependent, thereby requiring unique facilities to model the appropriate flow dynamics; and (*iii*) debris flow impacting a deformable structure is a highly non-linear problem that requires advanced numerical tools.

In this keynote paper, physical experiments that model the impact of dry sand, water, and two-phase debris flows on a rigid barrier are presented. Experiments were conducted using a 5 m-long flume and a 28 m-long flume. A numerical parametric study using the Material Point Method (MPM) was then carried out to investigate the effects of barrier flexural rigidity on the flow impact dynamics. Finally, design recommendations on debris flow impact are given.

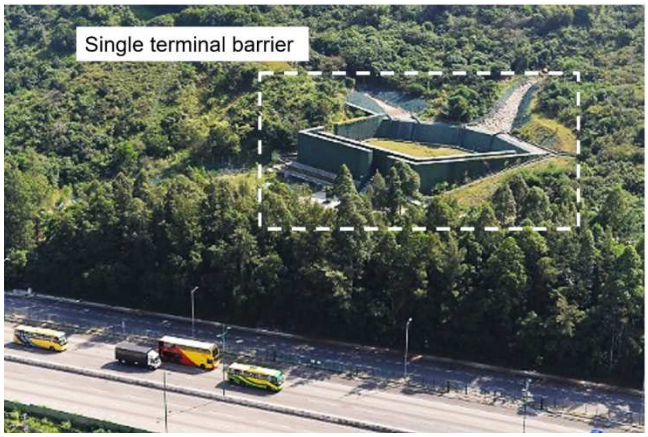

Figure 1. Rigid barrier in Hong Kong (HKO 2019).

2 PHYSICAL AND NUMERICAL MODELLING OF FLOW-BARRIER INTERACTION

2.1 Five-metre-long flume modelling

The 5 m-long flume was used to model the impact of dry sand and water on a rigid barrier. The 5 m-long flume has a rectangular cross-section with a width of 0.2 m and a depth of 0.5 m. A storage container with a volume of 0.06 m^3 is located at the upper end of the flume to hold the debris material, which is retained behind a pneumatically-controlled gate. The flow material in the 5 m-long flume was modelled using water or Toyoura sand, which has an average particle diameter of 0.2 mm. Fig. 2 shows a side view of the 5 m-long flume and the instrumentation layout. Flow kinematics were captured using high-speed cameras mounted at the side of the flume. Images with a resolution of 1300 × 1600 pixels were captured at a sampling rate of 640 frames per second. Images were then analysed using Particle Image Velocimetry (PIV) (White et al. 2003) to obtain the velocity fields. The instrumented model rigid barrier was assembled by sandwiching a load cell between an acrylic force plate and an aluminium reaction frame mounted inside the flume. The height of the model rigid barrier was 260 mm. The model barrier was installed at an inclined distance of 800 mm from the gate. Experimental plan and the flow parameters before impact using the 5 m-long flume are summarised in Table 1.

In each 5 m-long flume test, the barrier was installed in the flume, then the flow material was placed in the storage container. The flume was then inclined to the appropriate inclination angle. Finally, the gate was released to initiate the flows to impact the barrier.

Table 1. Experimental plan and flow parameters before impact for 5 m-long flume tests.

Test ID[a]	Flume inclination (°)	Flow velocity, v (m/s)	Flow depth, h_0 (mm)	Shear stress[b] (Pa)
W0	0	2.0	50	4.0×10^{-2}
W5	5	2.3	50	4.6×10^{-2}
W10	10	2.4	50	4.8×10^{-2}
W15	15	2.9	60	4.8×10^{-2}
S26	26	1.2	90	8.2×10^{2}
S35	35	1.5	100	9.1×10^{2}
S45	45	2.0	110	1.0×10^{3}

[a]W and S stand for tests using water and dry sand, respectively. The mass of water is 30 kg and the mass of dry sand is 100 kg.

[b]Shear stress for water is calculated by $\tau = \mu\dot{\gamma}$, where μ is the viscosity of water (0.001 Pa·s), and $\dot{\gamma}$ is the shear rate (v/h_0); shear stress for dry sand is calculated by $\tau = \rho g h_0 \tan\varphi$, where ρ is the density of dry sand (1680 kg/m^3), g is the gravitational acceleration (9.81 m/s^2), φ is the internal friction angle of dry sand (30°).

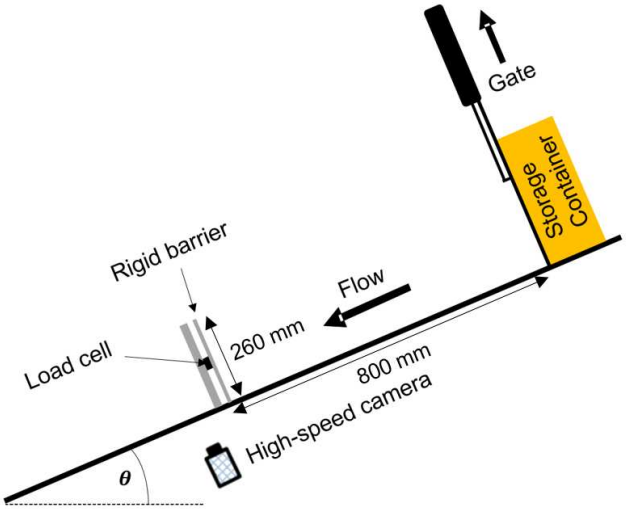

Figure 2. Five-metre flume setup with instrumentation.

2.2 Twenty-eight-metre-long flume modelling

The 28 m-long flume was used to model two-phase debris flows impacting a rigid barrier. Fig. 3 shows a front view of the flume model looking upstream. The flume has a uniform rectangular cross-section with a width of 2 m and a depth of 1 m. The side walls are transparent on one side of the flume. The rigid barrier consists of a steel plate mounted on a reinforced concrete structure. Four load cells were sandwiched between the steel plate and the reinforced concrete structure to measure the impact force. The steel plate is 1.5 m in height and 2.0 m in width. The rigid barrier was installed at a curvilinear distance of 17 m from the gate. The debris flow was modelled as a mixture of soil and water with a volume of 2.5 m^3 and solid fraction of 0.6. The soil mixture was 35% gravel (20 mm), 62.5% sand (0.6 mm), and 2.5% clay (< 2 μm). Details of the flume model, instrumentation, and debris materials are discussed in Ng et al. (2019).

In each 28 m-long flume experiment, the gates were secured and then the debris flow mixture was filled into the storage container. Afterwards, the gates were mechanically opened and the debris was allowed to discharge down the flume and impact the barrier.

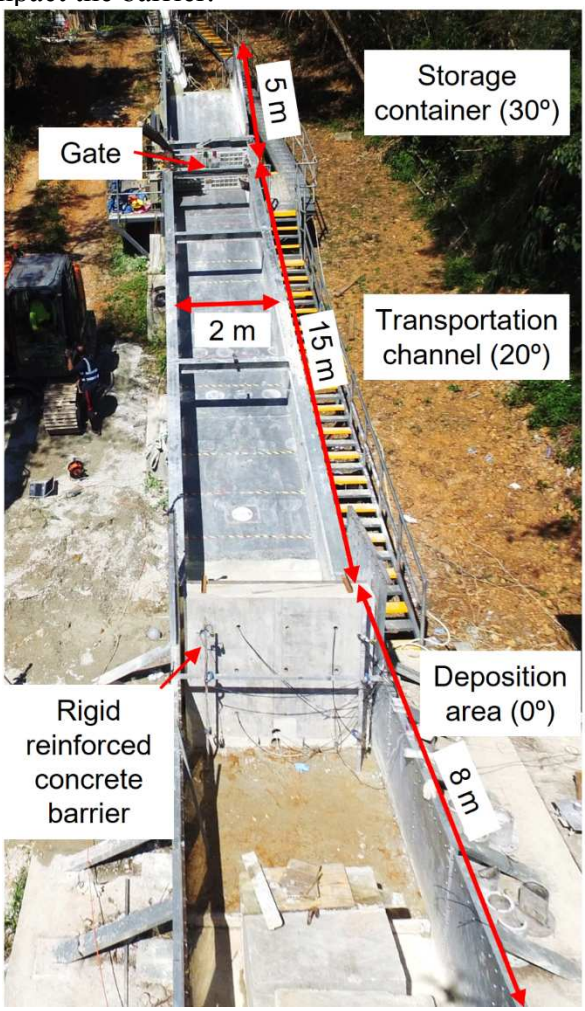

Figure 3. Front view of the twenty-eight-metre flume.

2.3 Material Point Method (MPM)

The MPM was adopted to model the impact dynamics of dry sand and water against barriers. The MPM discretizes the flow into material points. Each material point behaves according to a constitutive model. Each material point stores information of mass, velocity, stress and strain. At each time step, the information for each material point is mapped onto the nodes of a background mesh, which is used to deduce the velocity fields. The velocity is then extrapolated back to each material point to update its velocity and position. The dry sand was modelled as a linearly elastic

material with a Drucker-Prager yield criterion (Sołowski and Sloan 2015) and water was modelled as weakly compressible Newtonian fluid. Coulomb law (Bardenhagen et al. 2000; Nairn et al. 2017) was used to model the interface behaviour of the sand and the flume.

The numerical model setup is shown in Fig. 4. Two series of numerical simulations have been conducted. Firstly, water and dry sand impacting a rigid barrier were simulated to back analyse the 5 m-long flume tests as discussed in section 2.1. Secondly, the impact dynamics of dry sand against barriers with different flexural rigidities were modelled. A total of 30 kg of dry sand (Ng et al. 2017b), with a fairly uniform particle size of 0.6 mm was used. An interface friction coefficient of 0.4 was adopted based on laboratory measurements. The Young's modulus for the sand material was set to 1 MPa (Bui et al. 2008). A Poisson's ratio of 0.3 and an internal friction angle of 31° were adopted for the sand material. Young's moduli of 25 GPa and 160 GPa were used to model reinforced concrete and steel barriers, respectively. A typical 1 m-thick reinforced concrete barrier, with a flexural rigidity of 4.2×10^8 N·m^2, was modelled in the simulation to represent a rigid barrier. Barriers with lower flexural rigidities indicated by different equivalent thicknesses of reinforced concrete and steel were modelled. A summary of barrier flexural rigidities used in the numerical simulation plan is given in Table 2.

For each simulation, material points were generated in the container to represent flow material. Gravity was then applied to the computation domain to allow material points to reach static equilibrium in the storage container. The flume was then set to the target inclination and the gate was removed to allow the material to flow down the flume and impact the barrier.

Details of the numerical simulation plan, model calibration, constitutive model and input parameters for the MPM model are discussed in Ng et al. (2020a).

Table 2. Summary of flexural rigidity of barriers with equivalent materials.

E_bI_b	$3EI/H^3_{norm}$ [a]	Equivalent thickness of steel[b] (mm)	Equivalent thickness of reinforced concrete[b] (mm)
8.3	2.5×10^{-6}	2	5
3.3×10^2	1.0×10^{-4}	5	10
4.0×10^5	0.1	53	100
2.1×10^6	0.8	270	500
4.2×10^8	1.0	540	1000

Note: [a]$3EI/H^3_{norm}$ is the stiffness of cantilever barrier normalised by the stiffness of cantilever concrete barrier with a typical thickness of 1 m and height of 3 m;

[b]Young's moduli of steel and reinforced concrete are taken as 160 GPa and 25 GPa, respectively.

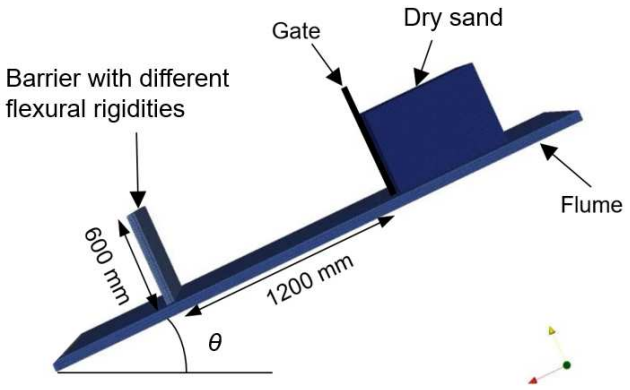

Figure 4. Numerical model setup.

3 OBSERVED IMPACT KINEMATICS

3.1 Dry sand and water impacting a barrier in the 5 m-long flume

The impact kinematics of dry sand and water on a rigid barrier installed orthogonally to the flume are shown in Figs. 5 and 6, respectively. The flume was inclined at 26° and 5° to model the dry sand (test S26) and water (test W5) impact, respectively. The observed kinematics from the high-speed camera are shown on the left and the corresponding velocity vectors from PIV analysis are shown on the right. For dry sand (Fig. 5), a tapered flow front reaches the barrier at t = 0.00 s. A dead zone forms at the base of the barrier and subsequent dry sand rides on top of the deposits. It can be seen that the dry sand deposits in layers towards the crest of the barrier (t = 0.50 s). At t = 1.00 s, the incoming flow is noticeably thinner due to a limited supply of sand material from the storage container. At t = 1.50 s, the barrier is filled to its crest. Each layer forms a shear interface between the incoming dry sand and deposited sand, causing energy dissipation. The dissipation of flow kinetic energy results in velocity reduction (Koo et al. 2017). This reduction is evident by examining the magnitude of the vectors deduced in the PIV analysis. For instance, the velocity reduces from 1.0 m/s to 0.5 m/s, which is a 50% decrease. Details of the velocity attenuation model during impact are

described and explained in Ng et al. (2019). The attenuated velocity was used by the authors to estimate the velocity of sand overflowing the barrier in their newly proposed multiple barrier framework. The overflow velocity can then be used to predict the landing distance (Kwan et al. 2015; Ng et al. 2018) and flow velocity after landing, thereby aiding the design of barrier spacing and impact force for multiple barriers.

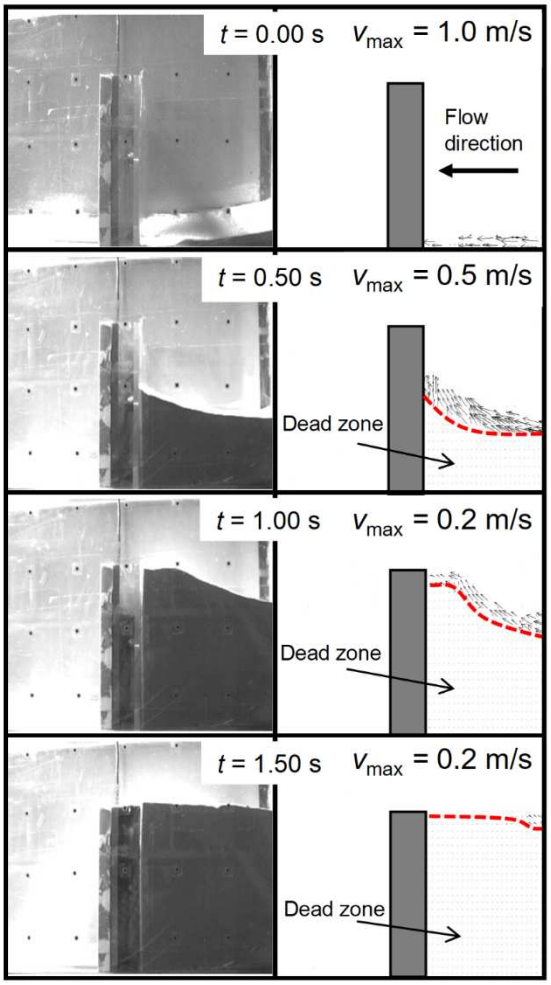

Figure 5. Observed impact kinematics and PIV analysis of dry sand in the 5 m-long flume (test S26).

Fig. 6 shows the water flow impacting on the barrier. At t = 0.15 s, the flow exhibits a vertical jet-like run-up (Choi et al. 2015) along the face of the rigid barrier and the velocity vectors show a 90° change in direction after impacting the barrier. The run-up height of the water exceeds the barrier height (t = 0.50 s). Overspill is observed at t = 1.00 s near the end of the impact process. Significant turbulence is observed as the water rolls-back and mixes with the incoming flow, indicating the dissipation of flow kinetic energy. In contrast to the 80% velocity reduction for dry sand (Fig. 5) the maximum velocity for water flow at t = 1.00 s (Fig. 6) only decreases by 50%. By comparing the impact behaviour between dry sand and water on a rigid barrier, the distinct differences in the impact mechanisms reveal the importance of flow material on impact dynamics. Ng et al. (2017a) conducted a series of centrifuge model tests to compare the impact dynamics of dry sand and viscous flows on a rigid barrier. It was reported that under similar pre-impact conditions, the impact force resulting from dry sand was about 2.5 times smaller than that of viscous flows. They explained that the impact dynamics of dry sand and water are mainly governed by frictional and viscous shear stresses, respectively. In this study, the frictional shear stress in dry sand is estimated to be four orders of magnitude higher than that of the viscous shear stress in water (see Table 1). It is evident that the energy dissipated by shearing of frictional contacts in dry sand is more significant compared to viscous shearing in water. Furthermore, the bulk compressibility of dry sand is much higher compared to that of water. High bulk compressibility results in larger volumetric strain, which extends the duration of shearing among grains. Shearing increases energy dissipation and leads to lower impact forces. More details of the impact mechanisms and the impact forces are discussed later.

3.2 Observed impact kinematics of two-phase debris flow in the 28 m-long flume

Fig. 7 shows a front view of the impact kinematics of a two-phase debris flow against a rigid reinforced concrete barrier (Ng et al. 2021). At t = 3.00 s, the flow reaches the base of the barrier. At impact, the flow jumps along the face of the barrier (Fig. 7a) and reflects upstream (Fig. 7b). The reflected flow mixes with the incoming flow (Fig. 7c). Eventually, the debris material reaches a static state (Fig. 7d). The observed impact kinematics of a two-phase debris flow against a rigid barrier exhibits a jet-like run-up impact mechanism, which is similar to the water flow observed in Fig. 6. The jet-like run-up of the two-phase debris flow is attributed to its fluidised nature, whereby frictional contact stresses are minimal (Ng et al., 2021).

4 IMPACT DYNAMICS ON THE BARRIER

4.1 Peak impact force

The peak impact force exerted on a barrier is the sum of the dynamic and static components from the flow as illustrated in Eqn. (1). The relative contributions of the dynamic and static forces to the peak force can be expressed in terms of the Froude number (Fr) of the flow before

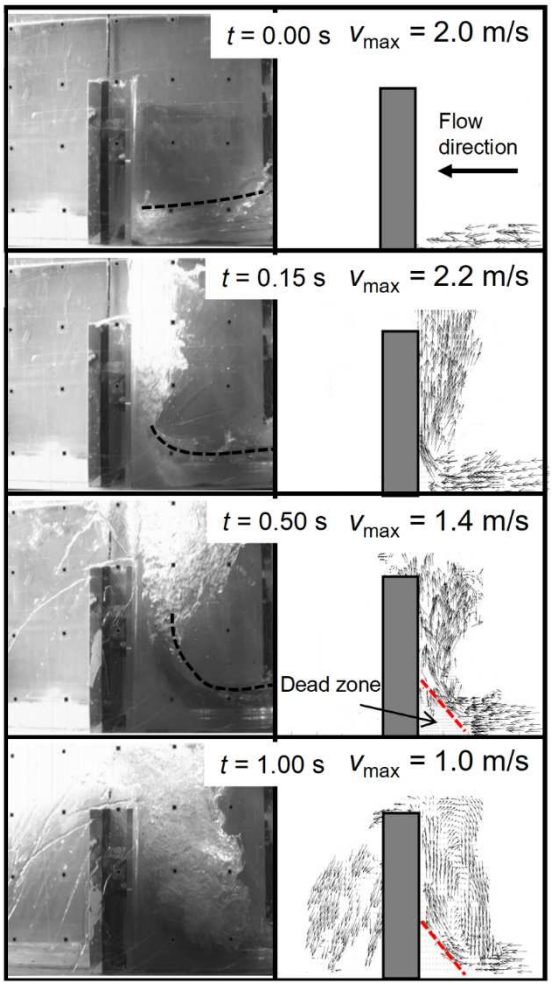

Figure 6. Observed impact kinematics and PIV analysis of water flow in the 5 m-long flume (test W5).

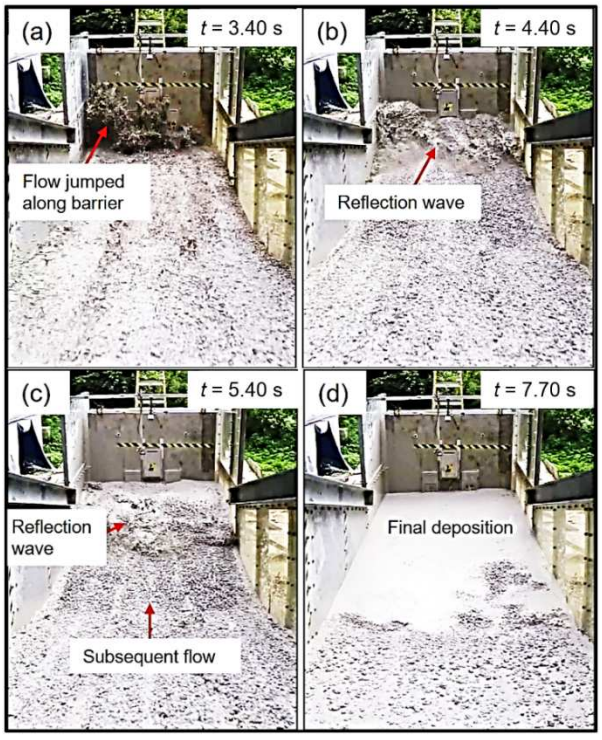

Figure 7. Observed impact kinematics of debris flow in the 28 m-long flume (Ng et al. 2021).

impact (Faug 2015). The Froude number of debris flow is strongly influenced by the geomorphological settings involved. For example, in Hong Kong, debris flows travel at high velocities on steep terrain over short distances. These conditions may lead to higher Froude numbers (Fr > 3). In contrast, the Froude conditions in the Alps or Rockies tend to be lower (Fr < 3) because the flows travel on gentler terrain.

Fig. 8 shows the relationship between the Froude number and the peak impact force F_{peak} (Eqn. 1) normalised by the theoretical static force $F_{static} = 0.5k\rho g h_0^2 w$ (Armanini and Scotton 1993; Armanini 2009) of the flow before impact. The normalised peak impact force is given as follows:

$$\frac{F_{peak}}{0.5k\rho g h_0^2 w} = 1 + \frac{2\alpha}{k} Fr^2 \qquad (2)$$

As discussed, design guidelines in Hong Kong adopt a large α value of 2.5 for rigid barriers (Kwan 2012) to account for hard and large inclusions. A theoretical static impact coefficient k = 1.0 is conservatively adopted in international guidelines (NILIM 2007; Kwan and Cheung 2012; Volkwein 2014) by assuming negligible internal shear strength of the debris material. These design parameters are used in Eqn. (2) and compared to the measured data. In addition, a recently proposed bounding line using Eqn. (2) by Ng et al. (2020b) is shown. The bounding line adopts k = 1.0 and α = 1.5. Details of the bounding line are discussed below.

It is clear from Fig. 8 that the measured impact forces of dry sand from Zanuttigh and Lamberti (2006), dry sand and water from this study, and two-phase debris flows from Ng et al. (2019) and this study all fall below the proposed bounding line (k = 1 and α = 1.5) by Ng et al. (2020b) for Froude numbers from 1 to 9. Moreover, the computed impact forces of dry sand and water on rigid barriers by MPM in this study are also below the proposed bounding line. Under a similar Froude number of about 7, the impact forces exerted by dry sand (Zanuttigh and Lamberti 2006) are lower compared to the impact forces exerted by two-phase debris flows in the 28 m-long flume tests. This is attributed to higher bulk compressibility and enduring frictional grain contacts in dry sand, leading to higher energy dissipation during the impact process (Choi et al. 2015). The higher energy dissipation of dry sand is also evidenced in the observed pile-up process during the impact (Fig. 5). On the contrary, the saturated two-phase debris flows were fluidised

and nearly incompressible (Fig. 7d), resulting in less significant energy dissipation during the impact process. The proposed bounding line captures the increasing trends of measured impact forces for both water and two-phase debris flows. The increasing trend may be also caused by the less energy dissipation during the impact of the water (Fig. 6) and two-phase (Fig. 7) debris flows compared with dry sand (Fig. 5). Evidently, the new bounding line provides a reasonable and conservative estimate of the peak impact force and can be used to optimise the design of rigid barriers in the future.

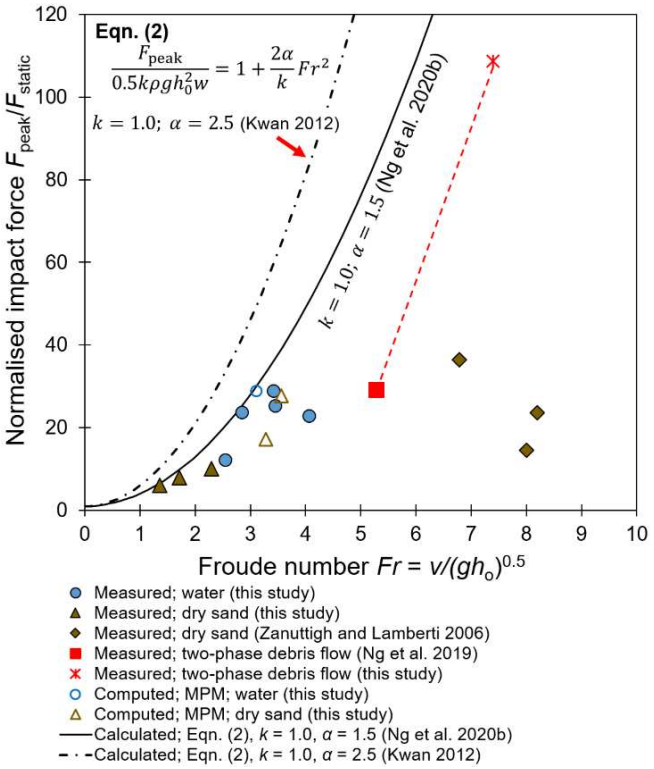

Figure 8. Relationship between Froude number and peak impact force.

4.2 Effects of barrier flexural rigidity

The impact behaviour of dry sand on barriers with different flexural rigidities (Table 2) are investigated using the MPM model (Section 2.3). Fig. 9 shows the effects of barrier flexural rigidity on the impact force normalised by the computed impact force on a 1 m-thick reinforced concrete barrier. The 1 m-thick reinforced concrete barrier is referred to as a rigid barrier. The maximum barrier deformation D_{max} along the direction of impact is normalised by the barrier height H. It is evident that the normalised impact force reduces nonlinearly as the flexural rigidity decreases. For instance, the use of a 2 mm-thick steel barrier ($3EI/H^3_{norm} = 2.5 \times 10^{-6}$) can reduce the impact force by 60% with deformation of 40% compared with a 1 m-thick reinforced concrete barrier. This result shows that by lowering the barrier stiffness, the peak impact force can be effectively reduced.

To understand the underlying mechanism that governs the impact force attenuation as flexural rigidity decreases, Figs. 10a and b show the comparison of the accumulated equivalent shear strain (ε_p) contours of the arrested dry sand mass behind the 2 mm-thick and the 5 mm-thick steel barriers, respectively. For the 2 mm-thick steel barrier, the larger deformation resulting from impact (refer to Fig. 9) causes the incoming flow to shear the deposited material more significantly compared with 5 mm-thick steel barrier, resulting in more distinct shear bands in the deposited material (Fig. 10a). In contrast, the accumulated equivalent shear strain is only noticeable along the boundaries for the arrested assembly of dry sand behind the 5 mm-thick steel barrier (see Fig. 10b). Within the deposit, the shear bands are not as pronounced as those observed for the softer 2 mm-thick steel barrier. The absence of distinct shear bands for the 5 mm-thick steel barrier reveals that the flow has experienced less shearing deformation after impact because of the smaller deflection of the stiffer barrier (as illustrated in Fig. 9). More discussion on the effects of shearing on energy dissipation and impact force is given later.

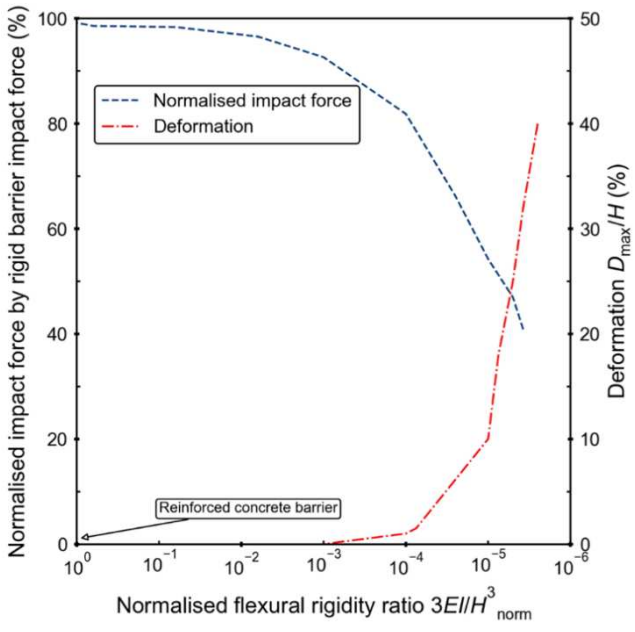

Figure 9. Relationship between barrier flexural rigidity and computed impact force of dry sand and barrier deformation.

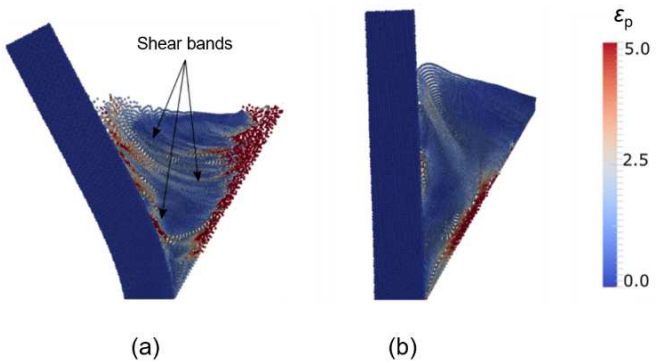

Figure 10. Computed equivalent shear strain (ε_p) inside dry sands: (a) 2 mm-thick steel barrier with $3EI/H^3_{norm} = 2.5 \times 10^{-6}$ and (b) 5 mm-thick steel barrier with $3EI/H^3_{norm} = 1.0 \times 10^{-4}$ (Ng et al. 2020a).

Fig. 11 compares the evolution of energy within a dry granular flow mass impacting the 1 m-thick reinforced concrete (RC) barrier ($3EI/H^3_{norm} = 1.0$) as well as another identical flow hitting the 2 mm-thick steel barrier ($3EI/H^3_{norm} = 2.5 \times 10^{-6}$), which are the largest and smallest barrier flexural rigidities simulated in this study. During a flow process, the total energy is composed of potential energy (PE), kinetic energy (KE) and total dissipative energy (TDE). Each type of energy is normalised by the initial PE (E_0) of the flow in the storage container prior to the initiation of each flow. The zero elevation reference for potential energy is defined at the toe of the barrier. In this study, TDE is a summation of frictional dissipative energy and internal dissipative energy. The frictional dissipative energy refers to the energy dissipated due to the friction between flow and boundaries. It is computed as the product of Coulomb friction force and sliding distance of the flow. The internal dissipative energy is computed from the plastic strain energy of the flow material, which is the integration of the product of stress and plastic strain over the entire flow body. The summation of frictional dissipative energy and internal dissipative energy is called total dissipative energy (TDE). The initial conditions of every flow are kept identical in each numerical simulation.

At t = 0.00 s, each flow is released from the container. As expected, the PE of each flow decreases and transfers into KE and TDE as the flow travels downslope. At t = 0.60 s, each flow attains the peak KE before impacting a barrier. After impact, the KE of the flow hitting on the 1 m-thick RC barrier and 2 mm-thick steel barrier decreases to zero at time t = 0.75 s and t = 0.85 s, respectively. The former impact has a shorter duration of attenuation than that of the latter one due to the difference in the flexural rigidity of the barrier. At the same time, the TDE within each flow increases sharply but reaches a plateau gradually when each flow is stopped by its corresponding barrier. After each impact at t = 1.00 s, the TDE of the flow impacting the 2 mm-thick steel barrier is 40% higher than that of 1 m-thick RC barrier. This is because the duration of impact at the more flexible steel barrier is 0.10 s longer than that of the flow which hits the rigid RC barrier. The larger deformation of 2 mm-thick steel barrier prolongs the interaction process between the flow and the barrier, as revealed in the delayed attenuation of KE during the impact. The higher TDE at the 2 mm-thick steel barrier is also attributed to the formation of shear bands as shown in Fig. 10. With more energy dissipated through intensive plastic shearing, the flow decelerates, resulting in a reduction of impact force acting on the steel barrier. Hence, a more deformable barrier can facilitate internal shearing of flow material to dissipate energy rather than absorbing all KE. This finding reveals that the use of the energy-based method (Sun and Law 2015), which does not consider the flexural rigidity of barrier, can be very conservative for the design of deformable barriers.

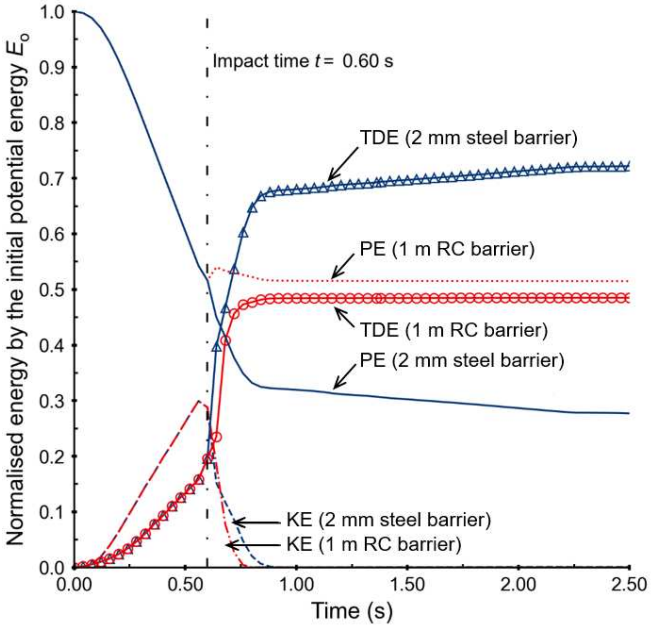

Figure 11. Computed energy evolution of dry sand impacting on barriers with two extreme flexural rigidities: 1 m-thick RC barrier and 2 mm-thick steel barrier.

5 SUMMARY AND CONCLUSIONS

In this keynote paper, experimental results of dry sand, water, and two-phase debris flows impacting a rigid barrier are presented.

Experiments were conducted at two different scales, including a 5 m-long flume and a 28 m-long flume. A numerical parametric study using the Material Point Method was carried out to examine the effects of barrier flexural rigidity on the impact dynamics of granular flow. Some key findings may be drawn as follows:

a) Based on the experimental data and numerical simulations in this study, it is recommended that the impact force acting on a rigid barrier should be estimated using $\alpha = 1.5$ and $k = 1.0$.

b) Barrier deformation enhances shearing in the granular assembly during impact. Internal plastic grain shearing facilitates energy dissipation when deformable barriers are used. For the two extreme cases investigated, the energy dissipation is more than 40% higher when the steel barrier is simulated than that of the rigid barrier.

c) The barrier with an equivalent flexural rigidity of a 2 mm-thick steel barrier can reduce the peak impact force by up to 60% as compared to the use of a 1 m-thick reinforced concrete barrier.

d) The use of the energy-based method, which does not consider the flexural rigidity of barrier, can be very conservative for the design of deformable barriers.

ACKNOWLEDGEMENTS

The authors are grateful for financial support from the theme-based research grant T22-603/15-N and area of excellence project grant AoE-E-603/18, as well as the general research fund grants 16212618, 16209717, and 16210219 provided by the Research Grants Council of the Government of Hong Kong Special Administrative Region, China. This paper is published with the permission of the Head of the Geotechnical Engineering Office and the Director of Civil Engineering and Development, the Government of the Hong Kong Special Administrative Region, China.

REFERENCES

Armanini, A. (2009). "*Discussion on: Experimental analysis of the impact of dry avalanches on structures and implication for debris flow (Zanuttigh, Lamberti)*". J Hydraul Res 47(3):381–383.

Armanini, A., Scotton, P. (1993). "*On the Dynamic Impact of a Debris Flow on Structures*". In Proceedings of XXV IAHR Congress, Tokyo (Tech. Sess. B, III), pp. 203–210.

Bardenhagen, S., Brackbill, J., Sulsky, D. (2000). "*The material-point method for granular materials*". Comput Methods in Appl Mech and Eng 187:529–41.

Bui, H.H., Fukagawa, R., Sako, K., Ohno, S. (2008). "*Lagrangian meshfree particles method (SPH) for large deformation and failure flows of geomaterial using elastic-plastic soil constitutive model*". Int J Num Anal Methods Geomech 32:1537–70.

Choi, C.E., Au-Yeung, S.C.H., Ng, C.W.W., Song, D. (2015). "*Flume investigation of landslide granular debris and water runup mechanisms".* Géotech Lett 5(1):28–32.

Faug, T. (2015). "*Depth-averaged analytic solutions for free-surface granular flows impacting rigid walls down inclines*". Physical Review E 92(6): 062310.

HKO. (2019). "*Educational Resources: Adapting to climate change – be prepared".* Hong Kong Observatory. Available from https://www.hko.gov.hk/climate_change/adapting_climate_change_e.htm [accessed 6 August 2019].

Koo, R.C.H., Kwan, J.S.H., Ng, C.W.W., Lam, C., Choi, C.E., Song, D., Pun, W.K. (2017). "*Velocity attenuation of debris flows and a new momentum-based load model for rigid barriers".* Landslides 14(2):617–629.

Kwan, J.S.H. (2012). "*Supplementary technical guidance on design of rigid debris-resisting barriers, Technical Note No. TN 2/2012".* Hong Kong, SAR China, Geotechnical Engineering Office, Civil Engineering and Development Department, The HKSAR Government.

Kwan, J.S.H., Cheung, R.W.M. (2012). "*Suggestions on design approaches for flexible debris-resisting barriers, Discussion Note No. DN 1/2012".* Hong Kong, SAR China, Geotechnical Engineering Office, Civil Engineering and Development Department, The HKSAR Government.

Kwan, J.S.H., Koo, R.C.H., Ng, C.W.W. (2015). "*Landslide mobility analysis for design of multiple debris-resisting barriers".* Can Geotech J 52(9):1345–1359.

Nairn, J.A., Bardenhagen, S.G., Smith, G.D. (2017). "*Generalized contact and improved frictional heating in the material point method*". Comput Part Mech 2017:1–12.

Ng, C.W.W., Choi, C.E., Koo, R.C.H., Goodwin, G.R., Song, D., Kwan, J.S.H. (2018). "*Dry granular flow interaction with dual-barrier systems".* Géotechnique 68(5):386–399.

Ng, C.W.W., Choi, C.E., Liu, L.H.D., Wang, Y., Song, D., Yang, N. (2017a). "*Influence of particle size on the mechanism of dry granular run-up on a rigid barrier*". Géotechnique Lett 7:79–89.

Ng, C.W.W., Song, D., Choi, C.E., Liu, L.H.D., Kwan, J.S.H., Koo, R.C.H., Pun, W.K. (2017b). "*Impact mechanisms of granular and viscous flows on rigid and flexible barriers*". Can Geotech J 54(2):188–206.

Ng, C.W.W., Choi, C.E., Majeed, U., Poudyal, S., De Silva, W.A.R.K. (2019). "*Fundamental framework to design multiple rigid barriers for resisting debris*

flows". In: Proceeedings of the 16th Asian Regional Conference on Soil Mechanics and Geotechnical Engineering. 14th to 18th October 2019. Taipei, Taiwan.

Ng, C.W.W., Wang, C., Choi, C.E., De Silva, W.A.R.K., Poudyal, S. (2020a). "*Effects of barrier deformability on load reduction and energy dissipation of granular flow impact*". Computers and Geotechnics 121: 103445.

Ng, C.W.W., Choi, C.E., Liu, H., Poudyal, S., Kwan, J.S.H. (2020b). "*Design recommendations for single and dual debris flow barriers with and without basal clearance*". In Workshop on World Landslide Forum (pp. 33-53). Springer, Cham.

Ng, C.W.W., Liu, H., Choi, C.E., Kwan, J.S.H., Pun, W.K. (2021). "*Impact dynamics of boulder-enriched debris flow on a rigid barrier*". J Geotech Geoenviron Eng 147(3): 04021004.

NILIM. (2007). "*Manual of technical standard for establishing Sabo master plan for debris flow and driftwood*". [In Japanese] Technical Note of NILIM.

Sołowski, W.T., Sloan, S.W. (2015). "*Evaluation of material point method for use in geotechnics*". Int J Numer Anal Methods Geomech 39:685–701.

Sun, H.W., Law, R.P.H. (2015) "*A preliminary study on impact of landslide debris on flexible barriers, Technical Note No. TN 1/2012".* Hong Kong, SAR China, Geotechnical Engineering Office, Civil Engineering and Development Department, The HKSAR Government.

Volkwein, A. (2014). "*Flexible debris flow barriers. Design and application".* WSL Berichte, 18. Birmensdorf, Swiss Federal Institute for Forest, Snow and Landscape Research WSL.

White, D.J., Take, W.A., Bolton, M.D. (2003). "*Soil deformation measurement using particle image velocimetry (PIV) and photogrammetry*". Géotechnique 53(7): 619–631. ICE Publishing.

Zanuttigh, B., Lamberti, A. (2006). "*Experimental analysis of the impact of dry avalanches on structures and implication for debris flows".* J Hydraul Res 44(4):522–534.